Supplemental Information to 'Statistics of chaotic resonances in an optical microcavity'

Li Wang[1], Domenico Lippolis[2,3], Ze-Yang Li[1], Xue-Feng Jiang[1], Qihuang Gong[1], and Yun-Feng Xiao[1]*
[1]*State Key Laboratory for Mesoscopic Physics and School of Physics, Peking University; Collaborative Innovation Center of Quantum Matter, Beijing 100871, China*
[2]*Institute for Advanced Study, Tsinghua University, Beijing 100084, China and*
[3]*Faculty of Science, Jiangsu University, Zhenjiang 212013, China*
(Dated: March 18, 2016)

This Supplementary Material is organized as follows. In Sec. I, we describe the boundary shape of the cavity and its unidirectional emission. In Sec. II, the Q factor magnitude distribution of the chaotic rays is estimated by ray-dynamics simulation. In Sec. III, we show geometry and field distribution of microtoroid by SEM images and finite element method modeling. In Sec. IV, power loss in the silica waveguide bonding with a thick silicon layer is studied. In Sec. V, we provide a cross-check that many high-Q modes do exist in the deformed microcavity by exciting them directly through a tapered fiber. In Sec.VI, the process of obtaining the number of high-Q regular modes is described. Sec. VII deals with the definition of the Ehrenfest time and rescaling of Lyapunov exponent in the Wey law. In Sec. VIII, we explain the χ^2 test used to assess the goodness of our fits. In Sec. IX, more experimental and fitting results are shown. Sec. X contains tables with the quantities and parameters used in our final results. In Sec. XI, the phase space with a small deformation factor together with the survival probability of a ray in the chaotic region are shown. In Sec. XII, we study the relation between the decay rates of WGMs and their coupling to chaotic modes.

I. BOUNDARY SHAPE OF THE CAVITY

The deformed microtoroid cavity in our experiment has a boundary shape given by the curve

$$\rho(\phi) = \begin{cases} \rho_0(1+\epsilon\sum_{i=2,3} a_i \cos^i\phi) & \text{for } \cos\phi \geq 0, \\ \rho_0(1+\epsilon\sum_{i=2,3} b_i \cos^i\phi) & \text{for } \cos\phi < 0, \end{cases} \tag{S1}$$

with $a_2 = -0.1329, a_3 = 0.0948, b_2 = -0.0642$, and $b_3 = -0.0224$. The WGMs in the deformed microcavity have been demonstrated to possess ultrahigh quality factors in excess of 10^8 in the 1550 nm wavelength band and to exhibit highly directional emission towards the 180° far-field direction, which emits tangentially along the cavity boundaries at polar angles $\phi = \pi/2$ and $\phi = 3\pi/2$. The deformation is controlled by $\eta = (d_{\max} - d_{\min})/d_{\max}$, $d_{\max}$ and $d_{\min}$, respectively, the maximum and minimum diameters of the cavity. The parameter η is related to ϵ through $\eta = \epsilon\,|a_2 + a_3 + b_2 - b_3|\,/2$. The η of cavity shape we used to draw the Poincaré surface of section in the main text is 11.7%.

II. ESTIMATING THE Q FACTOR MAGNITUDE DISTRIBUTION OF THE CHAOTIC RAYS

A ray-dynamics simulation is performed on the billiard with boundary set by Eq. S1 (ϵ=1). A swarm of initial points, randomly chosen in the chaotic region of the phase space, is iterated 1000 times. Each ray is considered to have escaped when it falls below the critical line of total internal reflection, and its quality factor Q is measured as $Q = 2\pi\tau\nu$, with τ lifetime of the ray and ν frequency of the light. The statistics shown in Fig. S1 indicates that Q is mostly of the order of 10^3, confirming the estimation from the experimental results.

III. GEOMETRY AND FIELD DISTRIBUTION OF THE MICROTOROID

The field localized at the boundary of the cavity (WGM) is shown in Fig. S2 (toroidal section). It can be seen that the toroid has little influence on the propagation of chaotic light fields into the disk part of the cavity since the

*Electronic address: yfxiao@pku.edu.cn; URL: www.phy.pku.edu.cn/∼yfxiao/

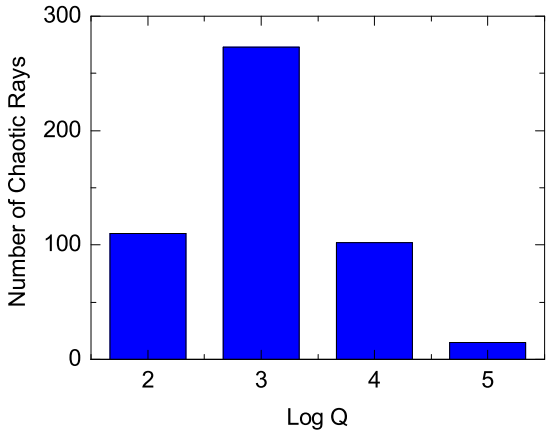

FIG. S1: Statistics of the quality factor for the chaotic rays in the deformed microcavity, from a ray-dynamics simulation.

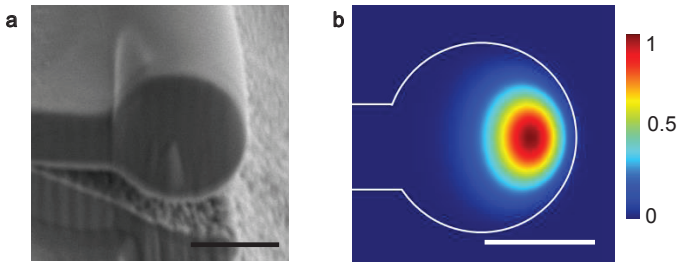

FIG. S2: (a) SEM cross-section image of the microtoroid. It is an oblique view taken by an angle of 56° with the horizontal direction. (b) COMSOL Multiphysics finite element method modeling of a fundamental TE mode. The white solid curve is the boundary of the cavity. The scale bar is 3 μm.

optical WGMs mainly locate at the same plane with the disk. This observation supports our two-dimensional model of the microcavity.

IV. POWER LOSS IN THE SILICA WAVEGUIDE BONDING WITH A THICK SILICON LAYER

The finite-element simulation in Fig. S3 shows that the power decrease sharply when the light propagates in the 2-μm-thick silica waveguide above a silicon layer with a sufficient thickness. In particular, the power decrease by 95% when propagating 20 μm (about 19 wavelengths). The wavelength of the light used here is 1550 nm. As for 635 nm wavelength, silicon has strong absorption, which may lead to a faster power decrease rate.

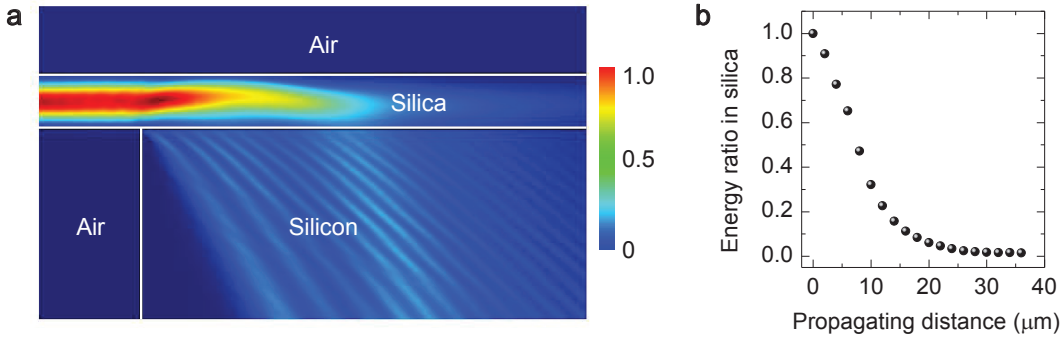

FIG. S3: (a) Finite-element-method modeling the light propagating inside the 2-μm-thick silica waveguide bonding with a thick silicon layer. (b) Remaining energy ratio in silica vs. the propagating distance.

V. FIBER TAPER AND FREE-SPACE COUPLING

In Fig. S4(a) we provide an independent cross-check that many high-Q modes ($Q > 10^5$) do exist in the deformed microcavity, by exciting them directly through a tapered fiber. Here the silicon pillar attached to the microtoroid has largest size, so that dynamical tunneling is inhibited and no WGM can be excited with the free-space coupling [Fig. S4(c)]. By reducing the size of the silicon pillar, as shown in Fig. 3 in the main text, high-Q modes can be excited indirectly by a free-space beam.

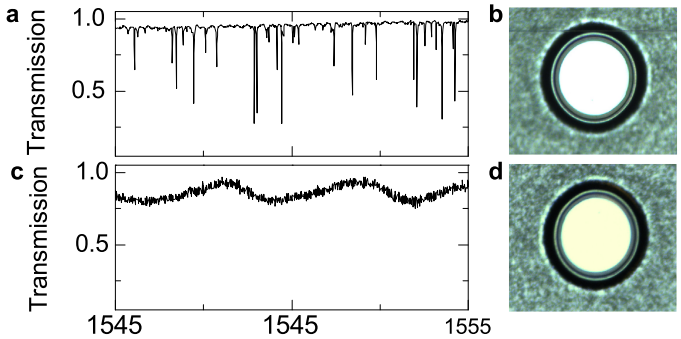

FIG. S4: Normalized transmission and top-view images of the cavity coupled by fiber taper [(a) and (b)] and free-space laser beam [(c) and (d)]. The absorber-to-cavity ratio $r \simeq 0.83$.

VI. COUNTING MODES IN TRANSMISSION SPECTRA

From the transmission spectra collected by the photon receiver, we single out the modes that have relatively high Q factors. In particular, we count those with $Q > 10^5$. There are TE modes and TM modes, which have orthogonal polarization in the microcavity. A polarization controller is used to excite modes with one polarization, adjust the polarization to alternatively achieve the highest efficiencies for one kind of modes and suppress the other one. We counted the number of modes in the transmission spectra with both kind of polarizations and add them together to obtain the total number of high$-Q$ regular modes. The so called TE modes and TM modes are not perfectly orthogonal in the real microcavity, so that some modes may be counted twice, which is the source of the uncertainty in our data.

VII. EHRENFEST TIME AND LYAPUNOV EXPONENT

We first give a brief explanation of how the semiclassical correction Eq. (4) of the main text was obtained in reference [39]. Our first goal is to estimate the fraction of trajectories that escape within the so called Ehrenfest time τ_{Ehr}, that is the time of quantum-to-classical correspondence. For an open system, τ_{Ehr} is the time it takes for a density as large as the size of the channels to be reduced to one Planck cell by the chaotic motion:

$$\frac{N}{M} e^{-\hat{\mu} t} = \frac{1}{M}, \tag{S2}$$

verified for $\tau_{Ehr} = \hat{\mu}^{-1} \log N$ (here $\hat{\mu}$ is proportional to the Lyapunov exponent of the closed system). Equation (S2) can also be thought of as the mean time it takes for a wavepacket the size of a Planck cell to escape, driven by classical dynamics. We notice τ_{Ehr} is proportional to the logarithm of the number of channels, meaning a faster escape implies a longer quantum-to-classical correspondence. Classically, the probability for an initial area A_0 of the phase space to survive for a time t is

$$P(t) \sim A_0 e^{-t/\tau_d}, \tag{S3}$$

so that the probability for an area to survive in the phase space within Ehrenfest time is simply $P(\tau_{Ehr}) \sim A_0 e^{-\tau_{Ehr}/\tau_d}$. Now take $A_0 = M$, total area of our phase space in units of h. From the definitions we gave of $\tau_{Ehr} = \hat{\mu}^{-1} \log N$,

we can express the survival probability at Ehrenfest time in terms of the number of open channels and Lyapunov exponent, as $N^{-1/\hat{\mu}\tau_d}$, and therefore the number of surviving modes as

$$M(\tau_{Ehr}) = MN^{-1/\hat{\mu}\tau_d}, \tag{S4}$$

as seen in Eq. (4) of the main text. In some sense, this is the 'real' Weyl law here, since its 'fractality' lies in the non-integral power.

The classical estimate of the prefactor MN^{-1/τ_d} involves Ehrenfest time, defined for *open* systems as

$$\tau_{Ehr} = \frac{1}{\mu}\log\frac{\tau_H}{\tau_d}. \tag{S5}$$

Here μ is the Lyapunov exponent of the closed system, τ_d is the dwelling time that we are already familiar with, while τ_H is the Heisenberg time

$$\tau_H = \frac{h}{\Delta E}, \tag{S6}$$

with ΔE mean level spacing, that is average distance (or difference) bewteen consecutive energy levels. We know, on the other hand, that $E = h\nu$, and we may therefore express Heisenberg time in terms of the frequency spacing

$$\tau_H = \frac{1}{\Delta\nu}, \tag{S7}$$

and Ehrenfest time as

$$\tau_{Ehr} = \frac{1}{\mu}\log\frac{N}{\Delta\Upsilon}. \tag{S8}$$

Here N is the number of open channels as we know, whereas $\Delta\Upsilon = MT\Delta\nu$, that is the mean frequency spacing times the Poincaré time (to make it dimensionless), times the number of states M. In plain words, $\Delta\Upsilon$ is the frequency range of our modes in units of the Poincaré time. At this point we can still write

$$\tau_{Ehr} = \frac{1}{\hat{\mu}}\log N, \tag{S9}$$

provided that

$$\hat{\mu} = \frac{\log N}{\log N - \log\Delta\Upsilon}\mu. \tag{S10}$$

Thus we have determined the rescaling to the Lyapunov exponent, following the definition of the Ehrenfest time.

We may give the rescaling factor an estimate, based on our experimental setup. Taking for example $T = \frac{a}{2c} \simeq 4\cdot 10^{-13}$s ($a$ is the diameter of the cavity, c the speed of light in the silica), $\lambda = 6.35\cdot 10^{-7}$m (visible light), the mean wavelength spacing (from the spectra) as $\Delta\lambda \sim 10^{-10}$m, we estimate $\Delta\nu = \frac{c\Delta\lambda}{\lambda^2} \sim 10^{11}$Hz. Moreover, the total number of states is estimated as $M \simeq Aa/\lambda \simeq 40$, with A area of the phase space in exam, while the mean number of open channels is estimated by the same expression with a smaller area, indicating the open strip of the phase space. Using the figures above, we get that

$$\hat{\mu} \simeq 1.3\mu. \tag{S11}$$

This correction turns out to be within the uncertainties of the average finite-time Lyapunov exponent numerically computed for the open billiard, and therefore it has been neglected.

VIII. χ^2 TEST

The expression for the χ^2 test used to assess the goodness of our fits is

$$\chi^2 = \frac{1}{\nu}\sum\frac{(x_{\rm ob} - x_{\rm th})^2}{\sigma^2}, \tag{S12}$$

$x_{\rm ob}$ being the observed datum, $x_{\rm th}$ its theoretical expectation, σ^2 the experimental uncertainty, and ν the number of degrees of freedom. In general, $\chi^2 \gg 1$ indicates a poor model fit, while $\chi^2 > 1$ indicates that the fit has not fully captured the data (or that the error variance has been underestimated). In principle, a value of $\chi^2 = 1$ indicates that the extent of the match between observations and estimates is in accord with the error variance. The limit of $\chi^2 < 1$ indicates that the model is over-fitting the data: either the model is improperly fitting noise, or the error variance has been overestimated.

IX. MORE EXPERIMENTAL AND FITTING RESULTS

In Fig. S5 we show more experimental and fitting results. Fig. S5(a)-(c) are in the infrared wavelength band and (d),(e) are in the visible wavelength band. All of them support our claim in the main text that the semiclassical correction (red solid curves) fits the experimental data better than the purely RMT-based estimate (blue dashed curves), especially at smaller deformation, where the two predictions differ the most.

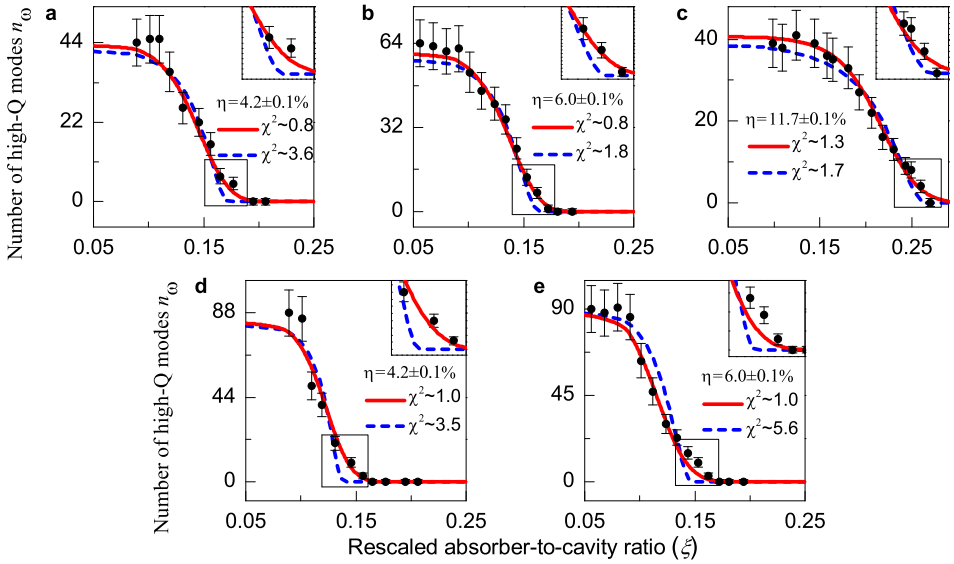

FIG. S5: (color online) Number of high-Q regular modes (n_ω) observed in the transmission spectra of the microcavity (Dots), as a function of rescaled absorber-to-cavity ratio ξ. Blue dashed and red solid curves are respectively RMT- and semiclassical prediction best fits. Here $\sin\theta_c \simeq 0.69$ and $\sin\theta_{\rm th} = 0.6$. Inset: the area where the two curves differ most.

X. TABLE OF PARAMETERS

We report the parameters used in our fittings in the following tables

TABLE I: Quantities used in relation to the RMT-based expression (Eq.(6) of the main text). γ is in unit of T^{-1}, with $T \simeq 4 \cdot 10^{-13}$s Poincaré time.

Γ	γ	η	λ(nm)	M	$\tilde{\chi}^2$
5.2	0.15	4.2%	630	40	3.5
3.2	0.19	4.2%	1550	20	3.6
7.2	0.16	6.0%	630	40	5.6
3.6	0.18	6.0%	1550	20	1.8
4.7	0.31	11.7%	1550	25	1.7

XI. PHASE SPACE WITH A SMALL DEFORMATION FACTOR

The phase space reported in the main text [Fig. 1(b)] belongs to a microcavity with relatively large deformation factor, $\eta = 11.7\%$. Here we report the classical phase space of the microcavity with the deformation factor $\eta = 4.2\%$ (Fig. S6), together with the survival probability of a ray in the chaotic region, obtained by analogously to the result shown in Fig. 5 of the main text. One can see here as well an overall algebraic decay of the survival probability, and a short-time (transient) hyperbolic behavior.

TABLE II: Quantities used in relation to the semiclassical prediction (Eq.(7) of the main text). Both γ and μ are in units of T^{-1}, with $T \simeq 4 \cdot 10^{-13}$s Poincaré time.

Γ	γ	η	λ(nm)	M	μ	$\tilde{\chi}^2$
2.9	0.19	4.2%	630	40	0.13	1.0
2.0	0.23	4.2%	1550	20	0.13	0.8
5.0	0.20	6.0%	630	40	0.15	1.0
2.5	0.21	6.0%	1550	20	0.15	0.8
1.5	0.38	11.7%	1550	25	0.21	1.3

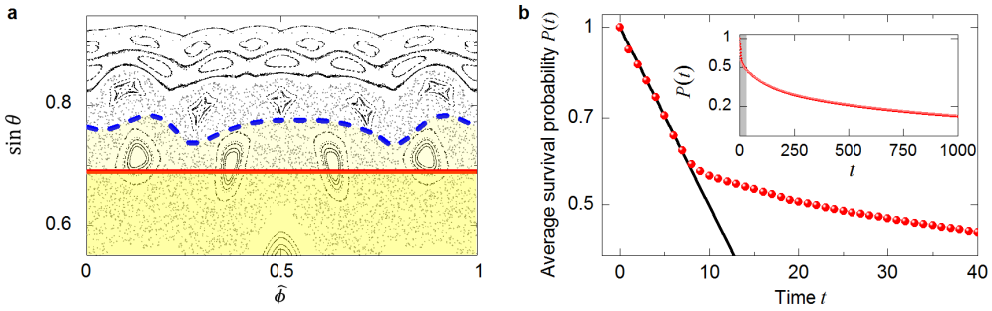

FIG. S6: (a) Poincaré surface of section of the microcavity with deformation factor $\eta = 4.2\%$. Red solid line indicates the angle of total internal reflection. (b) (logarithmic scale) Points: average survival probability $P(t)$ of a ray in the microcavity vs. t (in units of Poincaré time) at $\xi = 0.1$, from 10^6 randomly-started trajectories. Line: the ansatz $P(t) = \exp(-t/\tau_d)$, $\tau_d = 14$. Inset: the long-time simulation showing algebraic decay.

XII. DECAY RATES OF WGMS AND COUPLING TO CHAOTIC MODES

The approximations

$$\sum_n f_n \frac{V_n}{\gamma_n} \sim n_\gamma \frac{\bar{f}\bar{V}}{\bar{\gamma}}, \qquad \sum_n \frac{V_n^2}{\gamma_n} \sim n_\gamma \frac{\bar{V}^2}{\bar{\gamma}}. \tag{S13}$$

leading to Eq. (3) in the main text for the probability of excitation of a WGM may be thought of as too rough. In particular, the second expression in (S13) means that we are ignoring the fluctuations of both the coupling and the decay of the chaotic modes in consideration. In order to show that we are allowed to do so, we shall take a step back and rewrite the expression for the amplitude

$$a_\omega = \frac{E_0 \sum_n f_n \frac{V_n}{\gamma_n}}{[\gamma_\omega + i(\omega - \omega_0)] + \sum_n \frac{V_n^2}{\gamma_n}}. \tag{S14}$$

Here we recognize the total decay rate of the WGM of frequency ω as

$$\gamma_\omega^{tot} = \gamma_\omega + \sum_n \frac{V_n^2}{\gamma_n} \simeq \gamma_\omega + n_\omega \frac{\bar{V}^2}{\bar{\gamma}}, \tag{S15}$$

where the first term indicates the intrinsic linewidth of the WGM, while the second represents the decay into the chaotic modes. That already suggests that the larger n , the larger γ_{tot}. If we can really ignore the fluctuations γ_ω in V and γ, we should be able to see that trend. The problem is that we do not count n directly, and thus we need to express γ_{tot} in terms of some measurable quantity. A good candidate would be then n_ω, the number of excited WGMs. And that reminds us of another important approximation:

$$|a_\omega|^2 = \epsilon^2 \frac{n_\gamma^2}{\Gamma^2 + n_\gamma^2}. \tag{S16}$$

where κ is unknown. The assumption is that the number of excited WGMs is simply proportional to the probability of excitation of one WGM, where, in reality, $\Gamma = \gamma_\omega \bar{\gamma}/\bar{V}^2$ should be a function of ω, that is even the average coupling of each regular mode to the chaotic sea depends on where the mode is supported, in the phase space. It would appear from the literature on dynamical tunneling [e.g. A. Bäcker et al., Phys. Rev. Lett. 100, 104101 (2008)] that we are not allowed to ignore the dependence of Γ on ω as we did, since the couplings V stretch over several orders of magnitude, depending on the regular mode in question. Still, suppose for a moment we can go on making that approximation. Eq. (S15) would become, in terms of n_ω,

$$\gamma_\omega^{tot} = \gamma_\omega \left(1 + \sqrt{\frac{n_\omega}{\kappa - n_\omega}}\right) \tag{S17}$$

The advantage of this equation is that we have experimental data to fit it to. Figure S7 shows that Eq. (S17) does qualitatively capture the behavior of the average linewidths of the WGMs, within some errors. The fitted value for γ_ω corresponds to an average intrinsic Q factor of the order of 10^5, which is realistic. Importantly, the overall enlargement of the average linewidths with the number of observed WGMs constitutes independent evidence for the approximations leading to Eq. (S16) to be reasonable for our experiment.

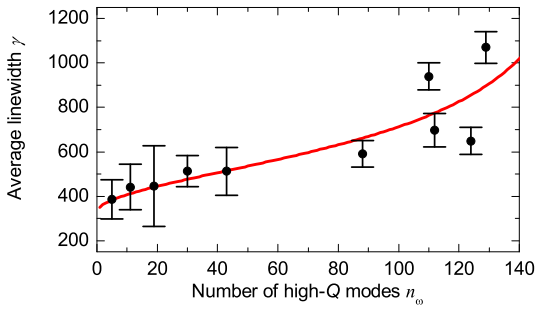

FIG. S7: Points: average linewidth of the excited WGMs vs. their number. Each data point represents one experiment with a different size of the silicon pillar. As we know, the number of observed WGMs increases as the size of the pillar decreases. Line: Eq. (S17), with $\gamma_\omega = 326$, and $\kappa = 171$.